REPORT DOCUMENTATION PAGE

Form Approved
OMB No. 0704-0188

1. REPORT DATE *(DD-MM-YYYY)*	2. REPORT TYPE	3. DATES COVERED *(From - To)*
January 2014	Journal Article	January 2014- August 2014

4. TITLE AND SUBTITLE

Homogeneous Media Milling: Reactant-Assisted Mechanochemical Synthesis of Functionalized Nanoparticles from Malleable and Ductile Metals

5a. CONTRACT NUMBER
In-House

5b. GRANT NUMBER

5c. PROGRAM ELEMENT NUMBER

6. AUTHOR(S)

Brandon W. McMahon, Jesus Paulo L. Perez, Jiang Yu, Jerry A. Boatz, Scott L. Anderson

5d. PROJECT NUMBER

5e. TASK NUMBER

5f. WORK UNIT NUMBER
Q188

7. PERFORMING ORGANIZATION NAME(S) AND ADDRESS(ES)

Air Force Research Laboratory (AFMC)
AFRL/RQRP
10 E. Saturn Blvd.
Edwards AFB, CA, 93524-7680

8. PERFORMING ORGANIZATION REPORT NO.

9. SPONSORING / MONITORING AGENCY NAME(S) AND ADDRESS(ES)

Air Force Research Laboratory (AFMC)

AFRL/RQR
5 Pollux Drive.
Edwards AFB, CA, 93524-7048

10. SPONSOR/MONITOR'S ACRONYM(S)

11. SPONSOR/MONITOR'S REPORT NUMBER(S)

AFRL-RQ-ED-JA-2014-163

12. DISTRIBUTION / AVAILABILITY STATEMENT

Approved for public release; distribution unlimited

13. SUPPLEMENTARY NOTES

14. ABSTRACT

A reactant-assisted mechanochemical method was used to produce copious nanoparticles from malleable/ductile metals, demonstrated here for aluminum, iron, and copper. Homogeneous Media Milling (HMM) generates metal nanoparticles via a reactant-accelerated wear process, where the reactant aids particle production by binding to the metal surfaces, enhancing particle production, and reducing the tendency toward mechanochemical (cold) welding. The mechanism is explored by comparing the effects of different types of solvents and solvent mixtures on the amount and type of particles produced. Particles were functionalized with oleic acid to aid in particle size separation, enhance dispersion in hydrocarbon solvents, and protect the particles from oxidation. For aluminum and iron, the result is air-stable particles, but for copper, the suspended particles are found to dissolve when exposed to air. Characterization was performed using electron microscopy, dynamic light scattering, Fourier transform infrared spectroscopy, and X-ray photoelectron spectroscopy. Density functional theory was used to examine the nature of carboxylic acid binding to the aluminum surface, confirming the dominance of bridging bidentate binding.

15. SUBJECT TERMS

16. SECURITY CLASSIFICATION OF:			17. LIMITATION OF ABSTRACT	18. NUMBER OF PAGES	19a. NAME OF RESPONSIBLE PERSON Jerry Boatz
a. REPORT Unclassified	**b. ABSTRACT** Unclassified	**c. THIS PAGE** Unclassified	SAR	45	**19b. TELEPHONE NO** *(include area code)* 661-275-5364

Standard Form
298 (Rev. 8-98)
Prescribed by ANSI
Std. 239.18

Homogeneous Media Milling: Reactant-Assisted Mechanochemical Synthesis of Functionalized Nanoparticles from Malleable and Ductile Metals

Brandon W. McMahon[†], Jesus Paulo L. Perez[†], Jiang Yu[†],

Jerry A. Boatz[‡a] and Scott L. Anderson[†a*]

[†]Chemistry Department, University of Utah, 315 S. 1400 E., Salt Lake City, UT 84112

[‡]Propellants Branch, Rocket Propulsion Division, Aerospace Systems Directorate, Air Force Research Laboratory, AFMC AFRL/RQRP, 10 E Saturn Blvd, Edwards AFB, CA 93524, USA

Abstract

A reactant-assisted mechanochemical method was used to produce copious nanoparticles from malleable/ductile metals, demonstrated here for aluminum, iron, and copper. Homogeneous Media Milling (HMM) generates metal nanoparticles via a reactant-accelerated wear process, where the reactant aids particle production by binding to the metal surfaces, enhancing particle production, and reducing the tendency toward mechanochemical (cold) welding. The mechanism is explored by comparing the effects of different types of solvents and solvent mixtures on the amount and type of particles produced. Particles were functionalized with oleic acid to aid in particle size separation, enhance dispersion in hydrocarbon solvents, and protect the particles from oxidation. For aluminum and iron, the result is air-stable particles, but for copper, the suspended particles are found to dissolve when exposed to air. Characterization was performed using electron microscopy, dynamic light scattering, Fourier transform infrared spectroscopy, and X-ray photoelectron spectroscopy. Density functional theory was used to examine the nature of carboxylic acid binding to the aluminum surface, confirming the dominance of bridging bidentate binding.

[*]Corresponding Author   [a]Senior Author

Keywords: Milling, wear, nanoparticle synthesis, aluminum, copper, iron, mechanochemistry

1. Introduction

Ball milling and related methods provide efficient means for particle production from bulk starting materials, and in the case of brittle materials, size reduction into the sub-100 nm range is possible.[1-3] The resulting size distribution is determined by the balance between fracturing to create smaller particles and mechanochemical "cold" welding, which tends to build up larger particles.[4-5] In a typical approach, micron or larger scale powder might be milled together with balls or other milling media of some hard material such as tungsten carbide, thereby being fractured into finer particles. For ductile and malleable materials, this approach can be inefficient, both because the particles are not readily fractured, and because mechanochemical welding is relatively efficient.[6-7]

Here, we report results from an alternative approach, which we will refer to as homogeneous media milling (HMM), which efficiently generates nanoparticles from malleable and ductile metals, via reactant-accelerated wear of particles from the surfaces of balls or other media composed of the metal of interest. The process quickly and simply generates grams of nanoparticles using inexpensive feedstock in a laboratory-scale mill, and should be adaptable to larger scale production. HMM also largely avoids an issue with conventional ball milling – that the products tend to become contaminated by material abraded or fractured from the milling media or jar walls, with contaminant levels increasing with milling time. Because the media is composed of the material of interest, which is softer than the milling vessel walls, contaminant levels in HMM are low.

The focus of this report is on understanding the mechanisms of HMM, i.e., the mechanisms for reactant-accelerated wear, and on optimizing conditions for production of particles, by controlling the particle surface chemistry. HMM particle production is explored in detail for the case of aluminum, which is not efficiently reduced to small nanoparticles in conventional ball milling.[8] The effects of different solvents and additives are used to probe the mechanism of particle production. The generality of the HMM approach is demonstrated by application to production of iron and copper nanoparticles.

2

The use of liquid reactants/adsorbates to enhance fracturing and wear has been examined for decades, since the early work of P. A. Rehbinder.[9] Nascent metal surfaces generated by fracturing have relatively high surface free energies,[7, 10] and adsorption of a strongly binding reactant lowers the energy, enhancing fracturing, and also reducing the tendency toward particle aggregation and cold welding.[10-11] Westwood *et al.*[12] discovered that the hardness of a material is at its maximum when the charge at the surface of the material is at a minimum (i. e. zero). Gayko *et al.*[13] reported a study that is probably the most closely related to what we are reporting here. They demonstrated the effects of adsorbates on size reduction in milling of aluminum powder with steel balls assisted by a variety of solvents. They discovered that the resulting size distribution shifted to smaller sizes when aluminum was milled in solvents that might be expected to adsorb strongly to aluminum (e.g. nitriles, alcohols, ketones), as opposed to solvents, such as hydrocarbons, which might be expected to interact weakly with the surface. Their study did not examine particles smaller than 20 μm, did not attempt to explore the effects of metal surface oxidation, and did not include measurements of the mode of adsorbate-surface binding. Here, we report a study that is focused on nanoparticle production, including spectroscopic and theoretical characterization of the resulting particle surfaces, and which examines the effects of surface oxidation and use of surface functionalization to control dispersibility in various solvents, both as a means to prepare stable suspensions, and to aid in size-separation. In particular, we demonstrate production of Al, Fe, and Cu nanoparticles capped *in situ* with oleic acid, to generate particles that are dispersible in hydrocarbons. Such particles are of interest as additives to hydrocarbon fuels.[14-20]

2. Materials and Methods

2.1 Safety considerations: The process described below has the potential to generate large quantities of unprotected, oxidizable nanoparticles, which spontaneously ignite upon exposure to air, water or other reactive species. All handling of milling feedstock and products is done inside an inert atmosphere glove box, and milling is done in a sealed jar, pressurized with inert gas to minimize air intrusion. Caution must also be exercised in choice of milling solvents and reactants. Some, such as alcohols or organic acids, may contain functional groups that react with the surfaces of the nascent nanoparticles, generating large volumes of hydrogen or other gases, which can pressurize the milling vessel to several atmospheres. We have also seen some evidence for HCN production in milling of reactive metals with nitrile-containing solvents. For safety, initial trials involving new reagents should be limited in volume, such that complete decomposition to gaseous products would not over-pressurize the milling vessel. Because of the potential for generation of reactive or toxic gases, provision should be made for controlled venting of the milling vessel, before the vessel is opened in an inert atmosphere, as described below.

2.2 Milling methodology: Particle production was done using a Retsch PM 400 planetary ball mill, and Retsch 250 ml tungsten carbide jars with custom-fabricated 316 stainless steel lids (supporting information Figure A1). The lids have the same dimensions as the original Retsch lids, but have a pair of threaded ports equipped with valves (McMaster-Carr part number 4912K96) that serve several purposes. The jars are loaded and sealed inside a N_2-filled glove box, which is equipped with a vacuum/pressure manifold that can be attached to the valves in the jar lid. To avoid potential reaction of N_2 with the nanoparticles under milling conditions, the manifold is used to pump out the N_2 after the jar is closed, and then backfill the jar with Argon (99.9999%) prior to milling. The manifold has a pressure/vacuum gauge that can be used for leak detection, and to check the jar pressure after milling. Milling solvents were degassed using a freeze-pump-thaw procedure, and stored in the glove box with activated 5 Å molecular sieves to remove any dissolved water. Solutions can be introduced into the jar via the valves by evacuating the jar with one valve

4

and drawing the solution in through the other valve. After filling, the sealed jar was removed from the glove box, and loaded into the mill. To allow direct comparison of different milling mixtures, all samples were prepared using identical milling parameters: three hours milling at 350 RPM sun wheel rotational frequency, corresponding to ~21 g relative centrifugal force. After milling, the jar was reintroduced into the glove box and attached to the pressure/vacuum manifold, allowing the headspace to be evacuated and exhausted into a fume hood. The jar was then opened in the N_2 atmosphere and the contents were removed, with particles washed from the milling media using an appropriate solvent.

2.3 Aluminum nanoparticle synthesis: Because aluminum is highly malleable and reactive, efficient production of aluminum particles is not straightforward, and many permutations of solvents and capping agent concentrations were investigated to provide insight into the factors that control efficiency of particle production by HMM. Aluminum milling was done using ~200 g of 8 mm aluminum balls and 100 ml of various solvent mixtures. After adding the balls, the jar was evacuated and purged, the solvent mixture was drawn into the jar, and finally the jar was pressurized with argon before being transferred out of the glove box for milling. All solvents were degassed by freeze-pump-thaw cycles, and stored in the glove box over molecular sieves.

The solvent that gave the best nanoparticle production was acetonitrile. In a typical process, aluminum balls were milled in 100 ml of acetonitrile for 3 hours at 350 rpm, generating copious particles, forming a dense slurry. For some experiments, the particles generated in acetonitrile were subsequently reacted with oleic acid to render them hydrocarbon-dispersible. For this purpose, we simply added oleic acid (3 ml) to the aluminum-acetonitrile slurry in the milling jar, and then milled for 15 min at 100 rpm to thoroughly mix the oleic acid into the aluminum-containing slurry, while minimizing production of additional particles. After interaction with oleic acid, the particles no longer were dispersible in acetonitrile, and precipitated out, allowing the acetonitrile to be decanted from the jar. The particles were found to be highly dispersible in

5

hydrocarbons, and therefore n-hexane was used to wash the particles out of the jar. Results for additional solvents and solvent mixtures are discussed below.

2.4 Unoxidized iron nanoparticle synthesis: Iron nanoparticles were generated by milling 3 mm diameter mild steel balls. Approximately 200 g of balls were loaded into the milling jar, which was then evacuated and purged with argon several times. The jar was then evacuated again, and 100 ml of 5% oleic acid in n-hexane was drawn into the jar, before finally pressurizing again with 55 psia of argon. The loaded jar was then milled at 350 rpm for 3 hours.

2.5 Oxidized iron nanoparticle synthesis: To produce oxidized iron nanoparticles, the jar was loaded with 200 g of steel balls and 100 ml of 5% oleic acid in n-hexane, and then sealed outside the glove box, with 1 atm. of laboratory air as the headspace atmosphere. This sample was also milled at 350 rpm for 3 hours.

2.6 Copper nanoparticle synthesis: Because we were unable to find inexpensive copper spheres, we tested production of copper particles by HMM using copper cylinders fabricated by simply cutting 6.35 mm diameter copper rod into a roughly 6 mm segments. The jar was filled with ~200 g of copper cylinders and 100 ml of a 5% oleic acid solution in n-hexane using the evacuation and argon purging method described above, then milled for 3 hours at 350 rpm.

3. Analysis: Particle sizes were characterized by a combination of electron microscopy and dynamic light scattering (DLS). DLS was performed using a NICOMP 380 ZLS instrument, with samples prepared by sonication in n-hexane for 30 min to disperse particles and break up aggregates. The concentration of the samples was adjusted by diluting in n-hexane until the dispersion was only slightly turbid. Size distributions were taken as the average of results from two 5 minute runs.

Scanning electron microscopy (SEM) was done using an FEI Nova Nano 600 instrument. Scanning transmission electron microscopy (STEM) was performed using an FEI Titan instrument operated at 200 kV. Samples were prepared for microscopy analysis using the same

6

dispersion/dilution procedure used in DLS, with the exception that samples were ultrasonicated just before drop casting on lacey carbon transmission electron microscopy (TEM) grids.

Fourier transform infrared (FTIR) spectroscopic experiments were performed using a Bruker Tensor 37 instrument, modified to collect light specularly reflected from the samples. The samples were drop casted onto a stainless steel stub, light from the IR source was focused onto the sample using an off-axis paraboloid, and light reflected from the sample was collected and refocused onto a mercury-cadmium-telluride detector with a spectral range of 4000 cm^{-1} to 850 cm^{-1}. The sample thickness was sufficient that the stainless steel stub was completely covered.

X-Ray photoelectron spectroscopy (XPS) was performed on a Kratos Axis Ultra instrument, using monochromatic Al Kα radiation (1486.6 eV) and an analysis area of 300 x 700 microns. Samples were prepared by drop casting onto stainless steel shims, and drying in air. Samples were placed in the instrument load-lock chamber and evacuated for a minimum of 12 hours by a turbo pump, to remove any volatile materials trapped in the sample matrix prepared by drop casting. Charging of the sample under X-ray irradiation was compensated using a low energy electron flood gun, tuned to optimize the sharpness of the XPS peaks. Spectra were analyzed using the Casa XPS program, and the binding energy scale was corrected to put the adventitious sp^2 carbon peak at 284.8 eV.[21-23]

To help understand the nature of oleic acid-aluminum binding, the interactions between aluminum nanoparticles and CH_3COOH were computed using density functional theory (DFT) methods with the M06 hybrid meta-generalized gradient approximation (GGA) exchange-correlation functional of Zhao and Truhlar.[24] The McLean-Chandler (12s,9p)/[6s,5p] contracted basis set[25], augmented with a d-type polarization function[26] and diffuse s+p shell[27], was used for aluminum and the 6-311++G(d,p) basis set [27-28] was used for carbon, oxygen, and hydrogen, with this combination of functional and basis sets henceforth denoted simply as M06/6-311++G(d,p). A cluster of 80 aluminum atoms, derived from a previously reported[29] calculated geometry of an 80-atom boron cluster with both exposed surface atoms and a bulk-like core, was used as a model for

7

an aluminum nanoparticle. All structures reported herein were fully optimized but have not been verified as local minima via diagonalization of the hessian matrix. All calculations were performed using the GAMESS[30] quantum chemistry program.

4. Results

4.1 Aluminum nanoparticles

In the process of optimizing aluminum nanoparticle production rates, many solvent/reactant mixtures were tried. Because they provide insight into the mechanism for particle production under HMM conditions, these initial results are summarized here. All aluminum milling was done in argon atmosphere, and all production methods described below used a liquid solvent or reactant, sometimes alone, and sometimes with oleic acid dissolved. In addition, in some experiments, particles were produced in a pure solvent, and subsequently functionalized with oleic acid.

For comparison, we also tried simply milling dry aluminum balls in an argon atmosphere for 3 hours at 350 RPM. The balls were first cleaned by milling in acetonitrile under argon, i.e., under conditions where the surface layer was removed in the form of particles (see below). The balls were then rinsed in acetonitrile, and dried in the N_2 glove box before loading into the milling jar. No nanoparticles were produced by dry milling in Ar. The balls were polished by the process, but also covered with ~1 millimeter facets, indicating peening by the energetic collisions in the mill. Evidently, if any particles were produced by dry milling, they were taken up again by the balls, presumably due to efficient cold-welding of the unoxidized aluminum particles to the unoxidized ball surfaces.

With the addition of an appropriate solvent, significant particle production can be observed, however, the amount and type of particles generated are strongly dependent on the milling mixture. The results of milling in 14 different solvents or mixtures are summarized in Tables 1 and 2. As reviewed by Bowmaker,[31] there are several working theories, but no agreed upon mechanism, for solvent-assisted mechanochemistry, reflecting the difficulties in obtaining molecular-level

8

information under chaotic reaction conditions. The variations seen for different solvents provide some insight, as discussed below.

Consider particle generation in several distinctly different classes of solvents or solvent mixtures, in each case milling 200 g aluminum balls in 100 ml of liquid for three hours at 350 RPM. As shown in Table 1, when milling in neat hydrocarbons, including both aliphatic and aromatic solvents, no detectable nanoparticles are produced. If these solvents are poured out of the mill into a sample container, the liquid is clear, and the only sign that milling occurred is the presence in some cases of a few (< 5 mg) large silvery flakes with dimensions in the >50 μm size range. See supporting information Figure A2a.

If Al balls are milled in 100 ml of neat oleic acid, a stable grey-black suspension of particles in oleic acid is recovered (see supporting information, Figure A2c). The high dispersibility, presumably, is due to some combination of particle surfaces being functionalized and oleic acid's high viscosity (>27,000 μPa·sec).[32-33] Upon centrifugation, ~5 g of large, silvery, metallic-appearing micron-size particles sedimented out. The supernatant liquid was deep black, suggesting that it contained a substantial concentration of nanoparticles. To recover these particles from the oleic acid suspension, the suspension was diluted with n-hexane, and then washed with ethanol. Oleic acid is quite soluble in ethanol, while the oleic-acid-functionalized particles were found to be highly dispersible in the n-hexane, as shown by the transfer of the black coloration into the hexane layer. The transferred particles were then dried, yielding approximately 100 mg of black nanoparticles. The amount is approximate because some nanoparticles were certainly lost in the centrifugation and washing process, and there also could still be excess oleic acid in the recovered material.

Table 1 also lists the results of milling with various concentrations of oleic acid in either toluene or hexane solvents, with hexane used for the highest concentration (0.16 M = 5% by volume). The production of micro- and nanoparticles was estimated by centrifugation, washing, and drying, as above. For low concentrations, only micron-size flakes are produced in measurable

9

quantities, but with increasing concentration, both micro- and nanoparticles are produced in reasonable quantities, with large flakes always dominating, by mass. Since nanoparticle production was similar for 0.16 M oleic acid in hexane and neat oleic acid, solutions with concentrations higher than 0.16 M were not investigated. It is interesting that oleic acid promotes particle production, because it is often included as an additive in lubricants, with the idea that metal surfaces are thereby coated with a strongly adhering, lubricating aliphatic layer.[34-35] For aluminum, at least, addition of oleic acid clearly greatly accelerates the wear rate, generating copious particles in both the nano and micron size regimes. This result is consistent with the proposal by Rehbinder[9] that adsorbates could lower the surface free energy, which might be expected to enhance surface creation by fracturing. In addition, surface functionalization might be expected to reduce the tendency toward cold welding[13, 36], which tends to heal fractures, and reattachment of particles to the ball surfaces.

We also milled in a series of polar/reactive solvents, including oleic acid, oleylamine, benzylamine, acetonitrile, ethanol, and dichloromethane, and the results are summarized in Table 2. Neat oleic acid, oleylamine and benzylamine resulted in qualitatively similar production of particles, generating two or more grams of large flake-like particles, but only ~10 mg to ~100 mg of nanoparticles. The most efficient nanoparticle production, and largest nano/micro particle ratio resulted from milling in neat acetonitrile, where more than a gram of nanopowder, along with more than a gram of large, micron size flakes were produced. Given the ease with which the nano and micron scale particles can be separated by sedimentation, this constitutes an efficient, inexpensive synthetic process. The efficient production of particles by milling with molecules expected to bind to the aluminum surface extends into the nanoscale, the observation by Gayko *et al.* that milling Al powder in surface-active solvents resulted in smaller particles, in the > 20 μm size range.

We also tried milling in ethanol despite the expectation that it might be too reactive with aluminum. There was copious gas generation, leading to pressurization of the milling jar to over 120 psia, at which point the o-ring seal failed. Upon opening the jar, it was found that most of the

10

ethanol had been consumed, and ~ 5 grams of white powder were recovered. Ethanol is known to decompose on aluminum surfaces, oxidizing the aluminum and producing hydrogen gas.[37] The fact that the powder was white indicates that the particles were completely oxidized, with no metallic core that would tend to absorb light. From the perspective of understanding the HMM mechanism, this experiment was useful, showing that particle production, albeit of oxide, was highly efficient in ethanol solvent.

Milling in dichloromethane (DCM) also led to reaction with the aluminum, generating a transparent yellow solution, which reacted violently with water to produce a white powder. The yellow solution was presumably a DCM solution of aluminum trichloride, which reacts with water to produce a white precipitate of aluminum chloride hexahydrate. Joly *et al.*[38] described the activation of C-Cl bonds in dichloromethane using density functional theory and electron paramagnetic resonance spectroscopy. Additional reports of aluminum activating the C-Cl bond of dichloromethane or carbon tetrachloride involve either a metal catalyst or elevated temperatures.[39-40] Here, we appear to be seeing reaction of aluminum with C-Cl bonds at milling jar temperatures below 100 ℃, however, several factors may enhance reaction under milling conditions. The local, instantaneous temperatures reached in collision of the balls have been speculated to be as much as two orders of magnitude higher than the bulk temperature,[8] and in addition, fresh unpassivated aluminum surfaces are constantly generated in the milling process, which may be highly reactive with DCM.   Nonetheless, catalysis by surfaces of the milling jar (cobalt-cemented tungsten carbide) or lid (316 stainless steel) cannot be excluded.

Because acetonitrile gave the most efficient nanoparticle production, it is worth describing in more detail. Aluminum balls milled in neat acetonitrile result in formation of a dense, black slurry. To stabilize the particles and aid separation, oleic acid was added to the acetonitrile suspension and milled briefly at low speed (100rpm), to thoroughly mix the slurry. After reaction with oleic acid, the particles precipitated out of the acetonitrile suspension, leaving a supernatant that was slightly cloudy and yellow in color, presumably reflecting the presence of impurities,

11

including aluminum particles too small to precipitate quickly. After pouring off the supernatant, the precipitated particles were readily dispersed in n-hexane, producing a dense black suspension (see supporting information, Figure A2b). Centrifugation of this suspension was used to separate out large particles (~1 g), from the nanoparticles remaining in suspension. These were then dried, resulting in ~1 g of nanoparticles.

The nanoparticle fraction suspended in n-hexane was diluted and analyzed by dynamic light scattering, and Figure 1 shows the result. As a control, DLS measurements were also performed on 5% oleic acid in n-hexane, confirming that oleic acid micelles were not giving rise to significant light scattering signal. The Al nanoparticle distribution is bimodal, with a sharp peak in the 5-10 nm range, and with ~24% of the total mass of nanoparticles in a broader feature centered around ~35 nm. There is also weak signal for particles in 250 - 500 nm range, indicating the presence of a small mass fraction corresponding to either aggregates of the small particles, or large particles that were not completely eliminated in the centrifugation step. Figure 2 shows the size distribution of the large particles from the sediments collected after centrifugation, resuspended in n-hexane. This suspension was not very stable, and was ultra-sonicated just prior to DLS data collection. There is a small peak (< 20 mass%) in the 500-900 nm range, but > 80% of the sediment mass consisted of particles greater than two microns in size, with the distribution cut off at three microns by the DLS instrument. Microscopic analysis of the particles is discussed below.

Comparison of the results for the various solvent mixtures suggests several factors that appear to control nanoparticle production rates. It is clear that solvents such as hydrocarbons, which do not interact strongly with aluminum surfaces, are ineffective for nanoparticle production. Conversely, solvents that contain functional groups that are too reactive with aluminum (e.g. ethanol, DCM) may aid particle generation, but also decompose and react with aluminum, generating salts or oxidized particles. Efficient nanoparticle production appears to require a solvent that interacts with aluminum, strongly enough to allow binding to the surfaces as they are exposed, but not so strongly that the solvent decomposes and converts the aluminum to an oxidized form.

12

The fact that acetonitrile is efficient for nanoparticle generation, but materials like oleic acid, oleylamine, or benzyl amine are not, unless they are diluted, suggests that viscosity may also play a role. Acetonitrile has similar viscosity to heptane (341 µPa·sec vs. 389 µPa·sec at room temperature),[41-43] but acetonitrile is polar and has unpaired electrons on the nitrogen that might be expected to result in a significant adsorption energy on unoxidized aluminum surfaces. Oleic acid has a carboxylic acid group that clearly binds strongly to aluminum, however, its viscosity is high (>27,000 µPa·sec),[32-33] as are those of oleylamine and benzylamine. Oleic-acid-capped nanoparticles can be generated by adding oleic acid to non-reactive solvents like toluene or n-hexane, however, nanoparticle production is more efficient if the aluminum is first milled in neat acetonitrile, with oleic acid added later.

Because acetonitrile was particularly effective at particle production, its mode of interaction with surfaces is of interest. We were unable to find any detailed studies of acetonitrile-aluminum binding, but Schwartz and Hamers[44] used XPS and polarized infrared analysis to study acetonitrile binding to silicon, reporting that the C=N bond was predominantly parallel to the Si (001) surface. This result suggested that the dative bond initially formed between the terminal N atom and the Si surface, was augmented by formation of an additional bond to either the α or β-carbon. FTIR studies by Schwartz and Hamers[45] on silicon and Filler et al.[46] on germanium found evidence for a ketenimine (C=C=N) stretch, and Schwartz and Hamers[45] also discuss the possibility of a less stable "(2 + 2)" adduct on the surface, where the α-carbon binds to the surface and results in an intact methyl group extending from the adduct (CH_3-C=N).

In the interest of better understanding the mechanism for aluminum particle production in HMM, microscopy was performed on the nanoparticles, the micron scale particles, and the ball surfaces before and after milling. As shown in Figure 3, the post-milling surface morphology of the balls is significantly different for different milling solvents, even when viewed at low magnification. All images show the surface of a ball removed after 3 hours of milling at 350 rpm, with fresh as-received balls used in each experiment, so as to avoid any residual structure from

13

prior milling. As shown in Figure 3a, the as-received balls are relatively smooth, with light pitting

and a few particles on the surface, which are most likely dust. After milling in neat toluene for 3

hours with an argon atmosphere (Figure 3b), the surface of the ball remained generally smooth, and

the density of small pits was lower than for the as-received ball. There is evidence, however, that

milling has worked the surface of the ball. The bright surface at the top left edge of the ball image

appears to be a spot where material has been spalled away. There are also millimeter scale

scratches observed on the surface of the ball, and dark spots which, in higher magnification, appear

to be particles with sizes greater than a micron on surface of the ball. Less than ~1 mg of flake-like

particles was recovered from milling in neat toluene, with sizes ranging from tens of microns to

about a millimeter. It is not clear if the particles observed adhering to the ball surface represent

particles in the process of being spalled from the surface, or in the process of being

mechanochemically welded (i.e., "cold-welded") back onto the surface of the balls, or both.

If oleic acid is added to the toluene, increasing particle production is observed, and as

might be expected, the surface of the ball shows more signs of wear (Figure 3c). There is

significantly more pitting, as well as large (> 100 μm) features that appear to be layers in the

process of exfoliation, which one might expect to give rise to flake-like particles. The brightness of

the edges of these features suggests differential charging from the electron beam, possibly

indicating that the edges are no longer in good electrical contact with the body of the ball. It seems

reasonable to assume that the micron scale flake-like particles observed in many of the milling runs

result from this exfoliation process, although it is possible that some of the adhering flakes result

from cold welding of previously generated flakes back to the surface of the ball.[47] It is not clear if

the small number of nanoparticles generated under these conditions also are generated by flaking of

micron size particles, following by grinding of the flakes into the nanoscale, or whether there is a

different process for direct ejection of nanoparticles from the surface. Figure 3d shows a ball

milled in neat acetonitrile, under conditions where roughly equal masses of large flake-like

particles and nanoparticles were generated. The ball surface is much rougher, and shows evidence

14

of both pitting and exfoliation. The difference among these samples tends to suggest that flake-like particles result from exfoliation, but that there may also be a process leaving pits on the ball surfaces that is correlated with efficient nanoparticle production.

To examine the structure of particles generated early in the milling process, Figure 4 shows a micrograph of a large flake collected after only 15 minutes of milling in acetonitrile. Note the evidence suggesting that this particle was in the process of exfoliating additional smaller flakes (circled region). The apparent curling of the left edge of the flake could be further evidence of exfoliation. Figure 5 shows nanoparticles that were extracted from the particle mixture after 3 hours of milling in acetonitrile, mixed with oleic acid, transferred to hexane, and then drop cast onto a TEM grid. The particle size distribution in this SEM image contains particles in the 30 – 200 nm size range. The main difference is that the SEM image shows no evidence of particles in the sharp DLS peak between 5 – 10 nm, however, such small particles of a low Z element may simply not have sufficient contrast to be resolved, particularly given that they are coated with oleic acid. To image these smaller particles, STEM was used, as shown in Figure 6, which shows the image of a group of particles, which individually have sizes below 20 nm. The faint, lighter gray layer on the surface of the particles is consistent with them being coated with an oleic acid layer.

To confirm that oleic acid is in fact covalently interacting with the particles, reflectance FTIR was performed, and Figure 7 compares the spectrum for aluminum nanoparticles capped with oleic acid (bottom), to that for neat oleic acid (top). For this experiment, the particle sample was washed three times with ethanol (in n-hexane suspension) to remove excess oleic acid. For neat oleic acid, strong absorption peaks are seen at 2854 cm^{-1} and 2925 cm^{-1}, corresponding to the symmetric and asymmetric CH_2 stretches of the sp^2 hybridized (aliphatic) regions of the backbone, as well as a weaker feature at 3004 cm^{-1} corresponding to the olefinic CH stretch associated with the double bond in the backbone.[48] The broad feature extending from 3600 cm^{-1} to 2400 cm^{-1} is assigned to the OH stretch, inhomogeneously broadened by hydrogen bonding in the liquid. Modes

15

associated with the COH group are located at 1413 cm^{-1} and 1286 cm^{-1},[49] and the most obvious

peak in the fingerprint region for neat oleic acid is the (C=O) stretch at 1713 cm^{-1}.[49]

The spectrum of the nanoparticles retains the CH$_2$ and olefinic CH stretch peaks of the

hydrocarbon tail, but the broad OH stretch band is largely absent. The OH bending mode at 1413

cm^{-1} is also absent, further suggesting that the OH group is involved in binding to the aluminum.

Most importantly, the C=O stretch peak (1713 cm^{-1}) in neat oleic acid is essentially absent in the

nanoparticle sample, and new peaks appear at 1608 cm^{-1} and 1468 cm^{-1} which are assigned to the

asymmetric and symmetric stretches of the now-equivalent CO bonds in the carboxylic acid head

group.[15, 50] Involvement of both oxygen atoms in binding to the aluminum is also suggested by the

absence of the COH mode at 1286 cm^{-1}.[51-52]

Clearly, the oleic acid is bonded to the surface of the aluminum particles via the acid head

group, and there are three possible binding arrangements. The first is a monodentate interaction in

which the OH moiety binds to aluminum, losing the H atom in the process. The IR spectrum for

this binding arrangement should have a strong peak at 1713 cm^{-1} from the uncomplexed C=O

group, and the near absence of this peak suggests that monodentate binding is a minor binding

arrangement for aluminum particles prepared in this way – not surprising given aluminum's high

affinity for oxygen. It is unclear whether the residual intensity at 1713 cm^{-1} results from a small

extent of monodentate binding, or if there was simply some residual uncomplexed oleic acid left

after repeated ethanol washing.

The other two configurations are both bidentate, and differ in that one has both O atoms in

the carboxylate group binding to a single aluminum atom ("chelating bidentate"), and the other has

the two O atoms binding to adjacent Al atoms ("bridging bidentate"). Wu *et al.*[53] have proposed

that the separation of the symmetric and asymmetric peaks CO stretching peaks can be used to

distinguish between chelating and bridging bidentate bonding. The bridging bidentate

configuration should result in asymmetric-symmetric stretch separation of 140 cm^{-1} to 190 cm^{-1},

while the chelating bidentate configuration should result in a smaller splitting between the two

16

peaks.[53] In our spectrum, the separation between the peaks is 140 cm^{-1}, which suggests that the dominant arrangement is bridging bidentate. Note, however, that there is a shoulder on the asymmetric stretch peak at 1581 cm^{-1}, and the separation of this shoulder from the symmetric stretch peak is only 105 cm^{-1}, suggesting that there may also be some chelating bidentate binding.[54]

Carboxylic acid binding to aluminum was studied using DFT, by calculating structures and energetics for acetic acid bound to the surface of an Al$_{80}$ cluster that possesses both surface atoms and bulk-like core atoms (Figure 8). To maintain charge neutrality, the acid proton was bound to a nearby aluminum atom. Consistent with the FTIR results, the bridging bidentate arrangement is found to be most stable, and the fact that the chelating bidentate arrangement is only ~7 kcal/mol higher in energy is consistent with the suggestion from FTIR that this structure may also be present to some extent. The monodentate interaction was calculated to be substantially higher in energy, again, consistent with the FTIR finding that monodentate binding makes little, if any, contribution to the binding. Note, however, that the DFT results are for a single acetic acid molecule on the surface, and it is certainly possible that the relative stability of the various binding arrangements would be changed in a saturated oleic acid layer on the surface.

To probe binding of adsorbates to the aluminum surface, and the oxidation state of the aluminum after air exposure, X-ray photoelectron spectroscopy (XPS) was used to examine samples of aluminum particles with, and without, oleic acid functionalization. Samples were dried and transferred to the XPS instrument in air, and then lightly Ar-sputtered to remove adventitious adsorbates, and implant Ar so that the Ar 2p$_{3/2}$ peak at 241.9 eV could be used for energy calibration.[21] Survey scans are included in the supporting information (Figure A3) for both aluminum milled only in acetonitrile (lower spectrum) and aluminum milled in acetonitrile and subsequently capped with oleic acid (upper spectrum). One point of interest is that there is no detectable W, Co, Fe, or other contaminants that might arise from the Co-cemented tungsten carbide jar or stainless steel lid. Not surprisingly, the carbon 1s peak dominates for the oleic acid-capped sample, both because oleic acid contains carbon, and because the presence of the capping

17

layer attenuates signal from the underlying particle. For the uncapped sample, the dominant peak is

O 1s, as expected for oxidized aluminum particles. The fact that the O 1s peak is larger than the Al

2s or 2p peaks, reflects the fact that the XPS sensitivity factor is ~3.7 times greater for O, compared

to Al.[55]

High resolution scans over the Al 2p peaks for the two samples are shown in Figure 9. For

the uncapped sample (9a), the spectrum is dominated by a high binding energy peak centered at

74.5 eV, which corresponds to Al in some oxidized form.[15, 56-59] There is also a weak shoulder at

lower binding energies, which is attributed to unoxidized Al in the core of the particles. The 72.0

eV binding energy for this feature is lower than expected for bulk aluminum (72.9 eV[55]), but there

is considerable uncertainty due to the weakness of the feature. The form of the oxidized aluminum

is not clear, but obvious possibilities are aluminum bound to oxygen and/or nitrogen (from

acetonitrile). For example, the 74.5 eV peak energy is within the ranges reported for both AlN and

Al_2O_3.[21, 56, 59-61]

In the spectrum for the oleic acid-capped sample (9b), several points are obvious. There is

roughly factor of three attenuation of the integrated aluminum signal, compared to that in the

uncapped sample, as expected due to scattering of aluminum photoelectrons as they pass through

the oleic acid layer. The spectrum for capped aluminum particles also shows features for oxidized

(74.5 eV) and unoxidized aluminum (72.9 eV), but clearly the relative intensity for the oxidized

aluminum is lower. For the uncapped spectrum the oxidized : unoxidized integrated intensity ratio

is ~9 : 1, dropping to ~2.5 : 1 for the capped sample, indicating that oleic acid is at least partially

passivating the particles with respect to air oxidation. As noted above, the 74.5 eV "oxidized"

feature may include contributions from aluminum bound to both N and O, and the latter is at least

partially due to binding of oleate to the aluminum surface.

Figure A6 in the supporting information shows the distribution of Al 2p binding energies

estimated using orbital energies from the DFT calculations. Distributions are shown for the Al_{80}

cluster, and for Al_{80} with a single acetic acid molecule bound in the three arrangements shown in

18

Figure 8. Because the DFT model system included only a single ligand molecule, and the estimation method does not include final state relaxation effect, the results are not directly comparable to experiment, however, they do show that binding of a single carboxylate leads to significant broadening of the Al 2p binding energy distribution. In particular, the one or two Al atoms involved in Al-O bonds are those with the highest binding energies, as expected.

High resolution scans for the C 1s and N 1s regions are shown in Figures A4 and A5 of the supporting information. For the uncapped sample, the C 1s spectrum is broad and weak (note x10 scaling). The carbon in this spectrum must originate from the acetonitrile used in milling and adventitious carbonaceous molecules. For the oleic acid-capped sample, the C 1s intensity is much greater, as expected, and the spectrum is dominated by a peak at 285 eV, which is assigned to carbon in the oleate layer. Because of unknown contributions from adventitious sources, more detailed assignment is not warranted. The N 1s spectra show that there is detectable nitrogen in both samples, and that neither the spectral features nor their intensities are strongly affected by capping. The main peak near 399 eV is consistent with organic nitrogen, and could result either from bound acetonitrile or adventitious molecules. The weaker ~397 eV feature is in the range expected for metal nitrides. Note, however, that if either of the N 1s features arises from N bound to the aluminum particles, we would expect that feature to be attenuated in the oleic acid-capped sample. The fact that the two spectra are so similar suggests that much of the nitrogen signal arises from adventitious sources, and therefore that nitride formation is probably not a significant contributor to the oxidized aluminum signal in Figure 9.

Figure 10 shows high resolution scans over the O 1s regions for both samples. The fact that the O 1s intensity is much weaker in the capped sample (note x2 scale factor) results from two factors. As shown by the Al 2p results in Figure 9, the aluminum in the capped sample is substantially less oxidized than in the uncapped sample. In addition, signal from oxygen present on the aluminum surfaces would be attenuated by passage through the capping layer. For the uncapped sample, the spectrum is well fit by a single peak centered at 531.3 eV which is assigned

19

to aluminum oxide (Al_2O_3)[62-63] The O 1s spectrum for the capped sample has contributions from at least two components, which is not surprising given that there may be oxygen from binding of oleate to the surface, from O_2 oxidation of the aluminum surface, and from adventitious sources.

In summary, the XPS results are consistent with binding of an oleate layer to the aluminum particle surfaces, which at least partially passivates the particles with respect to further oxidation upon air exposure. The XPS data also suggest that formation of either aluminum nitride or carbide during milling acetonitrile is not significant.

4.2 Iron and iron oxide nanoparticles produced in HMM

To investigate the generality of the HMM method, similar experiments were done for iron, i.e., a significantly harder, but still ductile metal. Iron nanoparticles were produced by milling steel balls in a 5% solution of oleic acid in n-hexane in Ar atmosphere. The resulting particles form a dense black suspension, which is stable with respect to settling out for at least 6 months. The size distribution was analyzed by DLS, and the mass-weighted (i.e., volume-weighted) results are given in Figure 11. The distribution is dominated by a peak in the 10 – 20 nm size range, and there is also a small component peaking near 600 nm, with essentially no signal for particles in the range between 20 and 400 nm. It is not clear if the 600 nm particles are aggregates of the small primary particles or if there are simply a few large particles present. In any case, their contribution to the particle distribution would only be a few parts per million on a number-weighted basis, and if desired, they can easily be separated out by centrifugation. Electron microscopy was used to investigate the particle morphology, as described in the supporting information (Figures A7 and A8, and associated text), resulting in particle sizes in reasonable agreement with the DLS results.

To confirm that oleic acid was actually binding to the iron, FTIR experiments analogous to those done for aluminum are reported in Figure A9 and associated discussion in the supporting information. As in the aluminum case, the spectrum of washed particles shows modes associated with CH stretches in the hydrocarbon tail, and for carboxylate CO stretches, but no significant intensity for OH or free C=O, suggesting that a bidentate interaction is dominant.

20

X-ray photoelectron spectroscopy was employed to look at the oxidation state of the different preparations of the iron nanoparticles. Supporting information Figure A10 shows survey spectra for both (a) argon-milled and (b) air-milled iron nanoparticles, both also milled with oleic acid and then ethanol-washed repeatedly to remove excess oleic acid. Supporting information Figure A11 shows the Fe $2p_{3/2}$ peak structure in more detail. Both sets of spectra are consistent with the air-milled sample being substantially oxidized, while the sample milled under Ar shows mostly metallic iron, along with smaller signal for partially oxidized iron which we attribute to binding of oleate to the iron surfaces.

4.3 Copper nanoparticles:

The experiments with copper provide another example of HMM of a ductile, malleable metal, but also test the necessity of using spherical milling media. Because we were unable to obtain copper balls at reasonable cost, we used 1:1 aspect ratio copper cylinders. Copper particles were produced using conditions that also resulted in reasonable production of particles for aluminum and iron. 200 grams of copper cylinders were milled with 100 mL of a 5% (0.16 M) solution of oleic acid in hexanes, at 350 rpm for 3 hours. The result was a copper-colored product containing approximately 15 grams of particles, many of which were in the >100 μm size range, easily seen with the naked eye. The large particles rapidly sedimented out of suspension, leaving a dense suspension of smaller particles which still appeared copper-colored, indicating the presence of particles in micron size range. These initial suspensions were stable for at least 1 hour, but upon centrifugation, could be separated further into particles in the few micron range which sedimented out, and a dense black suspension of nanoparticles (supporting information Figure A12a). DLS was used to probe this centrifuged nanoparticle suspension, resulting in a bimodal size distribution with one component centered at ~250 nm, making up ~ 7% of the total particle mass, with the remaining mass represented by a distribution centered at ~ 900 nm.

In the nitrogen glove box the suspended nanoparticles were stable for more than a week, but upon exposure of the suspensions to air they quickly (< 20 min) converted to a clear blue

21

solution which we attribute to formation Cu^{2+}, dissolved in hexane, presumably via interaction with oleic acid (supporting information Figure A12b). The conversion is surprisingly rapid, as shown by Figure A13 (supporting information) which gives a time history for dissolution of a dense suspension containing both nano and micro Cu particles. Since the suspensions are stable in hexanes in absence of air, it is clear that the copper particles are initially complexed by oleic acid. The rapid dissolution shows that the oleate layer does not passivate the surfaces against oxidation by atmospheric oxygen diffusing into the n-hexane solvent.

5. Discussion

HMM has the capacity to produce nanoparticles on the gram scale from inexpensive media. It is not possible to determine the mechanism of particle production in detail, but several aspects of the mechanism appear clear. The strong dependence of particle production on the nature of the milling solvent or solution, indicates that interaction between the metal surfaces and the solvent or solutes, is critical to particle production. In particular, particle production requires the presence of molecules which are able to bind to the metal surface, lowering the surface free energy as cracks propagate, and presumably inhibiting cold welding. High viscosity appears to inhibit production, particular of the nanoparticle fraction of the total particle mixture. For aluminum, microscopic examination of both the particles produced under various milling conditions, and the surfaces of the balls suggests that one mode of particle production involves exfoliation of flakes of materials, which may be further broken up by milling. The more extensive pitting of the balls under conditions where nanoparticle production is high suggests that there may also be a second mechanism that correlates with nanoparticle generation.

From the perspective of the mechanism for nanoparticle production, it is useful to consider the full size distribution for aluminum milled in acetonitrile, under conditions where both nanoparticles and micron-scale flakes are generated in roughly equal amounts. The nanoparticle portion of the distribution consists mainly of particles in the 5 to 10 and 20 to 50 nm size ranges, with much weaker signal (24% of the nanoparticle mass) in the 250 nm to 500 nm range. DLS of

22

the large particles sedimented out of the initial distribution shows a small feature in the 500 to 900 nm range, but the bulk of the large particles are flake-like, and larger than 2 microns, as confirmed by SEM analysis. If the only mechanism for nanoparticle production were breaking up large flakes, one might expect that the size distribution should be more continuous than the observed distribution, where there is a large gap with negligible particle mass between 50 and 250 nm, and a smaller gap between 900 nm and 2.5 microns.

In general, the distribution of particles produced by homogenous media milling is expected to reflect a balance between wear processes that spall or abrade particles from the media surfaces, and cold welding, which tends to build up larger particles and reattach particles to the media surfaces. Binding of surface-active molecules to the media surfaces enhances the net wear rate, indicating that the effects of adsorption on surface free energy and cold welding, outweigh any lubricating effect that might be expected from binding of molecules like oleic acid to the surface. The SEM images suggest that at least for the micron size flakes, exfoliation may occur by gradual separation as the crack between the flake and media surface propagates under repeated impacts. In that case, the presence of molecules that bind strongly to the nascent surfaces may substantially enhance exfoliation by coating the inner surfaces of the propagating crack, reducing the free energy of the crack surfaces and the propensity for subsequent impacts to cold-weld the crack shut. The same effect would presumably help nascent particles avoid being welded together to increase particle size, and being welded back onto the surface of the media.

Associated Content

Supporting Information

Additional XPS, FTIR, and electron microscopy data are presented, along with a schematic drawing of the milling jar lid, additional DFT computational results, and photographs of various particle suspensions, and the reaction of copper particles with air. This material is available free of charge via the Internet at http://pubs.acs.org/.

Author Information

23

Corresponding Author

* Tel: (+1) 801-585-7289, Email: anderson@chem.utah.edu

Author Contributions:

J. A. B. and S. L. A. are senior authors.

Notes

The authors declare no competing financial interest.

<u>**References**</u>

(1)   Van Devener, B.; Perez, P.; Jankovich, J.; Anderson, S., Oxide-Free, Catalyst-Coated, Fuel-Soluble, Air-Stable Boron Nanopowder as Combined Combustion Catalyst and High Energy Density Fuel. *Energy Fuels 2009* **2009,** *23*, 6111–6120.

(2)   Can, M. M.; Ozcan, S.; Ceylan, A.; Firat, T., Effect of Milling Time on the Synthesis of Magnetite Nanoparticles by Wet Milling. *Materials Science and Engineering: B* **2010,** *172*, 72-75.

(3)   Bonetti, E.; Bianco, L. D.; Pasquini, L.; Sampaolesi, E., Thermal Evolution of Ball Milled Nanocrystalline Iron. *Nanostructured Materials* **1999,** *12*, 685-688.

(4)   Suryanarayana, C., Mechanical Alloying and Milling. *Prog. Mater. Sci.* **2000,** *46*, 1-184.

(5)   Eckert, J., Relationships Governing the Grain Size of Nanocrystalline Metals and Alloys. *Nanostructured Materials* **1995,** *6*, 413-416.

(6)   Hebda, M.; Gądek, S.; Kazior, J., Thermal Characteristics and Analysis of Pyrolysis Effects During the Mechanical Alloying Process of Astaloy Crm Powders. *Journal of Thermal Analysis and Calorimetry* **2012**.

(7)   Gutman, E. M., *Mechanochemistry of Materials*. Cambridge International Science Publishing: Cambridge, 1998;

(8)   Balaz, P.; Achimovicova, M.; Balaz, M.; Billik, P.; Cherkezova-Zheleva, Z.; Criado, J. M.; Delogu, F.; Dutkova, E.; Gaffet, E.; Gotor, F. J.; Kumar, R.; Mitov, I.; Rojac, T.; Senna, M.; Streletskii, A.; Wieczorek-Ciurowa, K., Hallmarks of Mechanochemistry: From Nanoparticles to Technology. *Chemical Society Reviews* **2013,** *42*, 7571-7637.

(9)   Rehbinder, P. A., Reports at the Vi Conference of Russian Physicists. 1928

(10)   Ryou, J., Improvement on Reactivity of Cementitious Waste Materials by Mechanochemical Activation. *Mater. Lett.* **2004,** *58*, 903-906.

(11)   Ding, H.; Zhou, H.; Zheng, Y. X.; Wang, M. M., Effect of Sodium Stearate on Grinding Behaviour of Calcium Carbonate in Wet Stirred Mill. *Materials Research Innovations* **2013,** *17*, 292-296.

(12)   Westbrook, J. H.; Conrad, H.; Metals, A. S. f., *The Science of Hardness Testing and Its Research Applications*. American Society for Metals: 1973;

(13)   Gayko, M.; Wuestefeld, B.; Wochnowski, H., Effect of Sorption and Reaction Processes on the Strength of Metals and the Effect of Sorptively Generated Tribologic Properties on the Kinetics of Comminution. *Z. Phys. Chem. (Frankfurt am Main)* **1973,** *87*, 82-93.

(14)   Lee, S. Y.; Harris, M. T., Surface Modification of Magnetic Nanoparticles Capped by Oleic Acids: Characterization and Colloidal Stability in Polar Solvents. *Journal of Colloid and Interface Science* **2006,** *293*, 401-408.

(15)   Lewis, W. K.; Rosenberger, A. T.; Gord, J. R.; Crouse, C. A.; Harruff, B. A.; Fernando, K. A. S.; Smith, M. J.; Phelps, D. K.; Spowart, J. E.; Guliants, E. A.; Bunker, C. E., Multispectroscopic (Ftir, Xps, and Tofms-Tpd) Investigation of the Core-Shell Bonding in Sonochemically Prepared Aluminum Nanoparticles Capped with Oleic Acid. *J. Phys. Chem. C* **2010,** *114*, 6377–6380.

(16)   Guardia, P.; Labarta, A.; Batlle, X., Tuning the Size, the Shape, and the Magnetic Properties of Iron Oxide Nanoparticles. *J. Phys. Chem. C* **2010,** *115*, 390–396.

(17)   Jeng, J. Y.; Liu, J. C.; Jean, J. H., Dispersion of Oleate-Modified Cuo Nanoparticles in a Nonpolar Solvent. *Journal of the American Ceramic Society* **2007,** *90*, 3676-3679.

(18)   Bunker, C. E.; Karnes, J. J., Low-Temperature Stability and High-Temperature Reactivity of Iron-Based Core-Shell Nanoparticles. *J. AM. CHEM. SOC.* **2004,** *126*, 10852-10853.

(19)   Gan, Y.; Lim, Y. S.; Qiao, L., Combustion of Nanofluid Fuels with the Addition of Boron and Iron Particles at Dilute and Dense Concentrations. *Combustion and Flame* **2012,** *159*, 1732-1740.

(20)   Beloni, E.; Hoffmann, V. K.; Dreizin, E. L., Combustion of Decane-Based Slurries with Metallic Fuel Additives. *Journal of Propulsion and Power* **2008,** *24*, 1403-1411.

(21)   Moulder, J. F.; Stickle, W. F.; Sobol, P. E.; Bomben, K. D., *Handbook of X-Ray Photoelectron Spectroscopy*. Perkin-Elmer Corporation Eden Prairie, 1992; p 261.

(22)   Frydman, E.; Cohen, H.; Maoz, R.; Sagiv, J., Monolayer Damage in Xps Measurements as Evaluated by Independent Methods. *Langmuir* **1997,** *13*, 5089-5106.

26

(23)   Hanumantha, P. J.; Datta, M. K.; Kadakia, K. S.; Hong, D. H.; Chung, S. J.; Tam, M. C.; Poston, J. A.; Manivannan, A.; Kumta, P. N., A Simple Low Temperature Synthesis of Nanostructured Vanadium Nitride for Supercapacitor Applications. *J. Electrochem. Soc.* **2013,** *160*, A2195-A2206.

(24)   Zhao, Y.; Truhlar, D. G., The M06 Suite of Density Functionals for Main Group Thermochemistry, Thermochemical Kinetics, Noncovalent Interactions, Excited States, and Transition Elements: Two New Functionals and Systematic Testing of Four M06-Class Functionals and 12 Other Functionals. *Theor. Chem. Acc.* **2008,** *120*, 215-241.

(25)   McLean, A. D.; Chandler, G. S., Contracted Gaussian Basis Sets for Molecular Calculations. I. Second Row Atoms, Z = 11-18. *J. Chem. Phys.* **1980,** *72*, 5639-48.

(26)   Francl, M. M.; Pietro, W. J.; Hehre, W. J.; Binkley, J. S.; Gordon, M. S.; DeFrees, D. J.; Pople, J. A., Self-Consistent Molecular Orbital Methods. Xxiii. A Polarization-Type Basis Set for Second-Row Elements. *J. Chem. Phys.* **1982,** *77*, 3654-65.

(27)   Clark, T.; Chandrasekhar, J.; Spitznagel, G. W.; Schleyer, P. v. R., Efficient Diffuse Function-Augmented Basis Sets for Anion Calculations. Iii. The 3-21 + G Basis Set for First-Row Elements, Lithium to Fluorine. *J. Comput. Chem.* **1983,** *4*, 294-301.

(28)   Krishnan, R.; Binkley, J. S.; Seeger, R.; Pople, J. A., Self-Consistent Molecular Orbital Methods. Xx. A Basis Set for Correlated Wave Functions. *J. Chem. Phys.* **1980,** *72*, 650-4.

(29)   Perez, J. P. L.; McMahon, B. W.; Yu, J.; Schneider, S.; Boatz, J. A.; Hawkins, T. W.; McCrary, P. D.; Flores, L. A.; Rogers, R. D.; Anderson, S. L., Boron Nanoparticles with High Hydrogen Loading: Mechanism for B-H Binding and Potential for Improved Combustibility and Specific Impulse, *ACS Applied Materials & Interfaces*, in press.

(30)   Schmidt, M. W.; Baldridge, K. K.; Boatz, J. A.; Elbert, S. T.; Gordon, M. S.; Jensen, J. H.; Koseki, S.; Matsunaga, N.; Nguyen, K. A.; et, a., General Atomic and Molecular Electronic Structure System. *J. Comput. Chem.* **1993,** *14*, 1347-63.

(31)   Bowmaker, G. A., Solvent-Assisted Mechanochemistry. *Chem Commun (Camb)* **2013,** *49*, 334-48.

(32)   Valeri, D.; Meirelles, A. J. A., Viscosities of Fatty Acids, Triglycerides, and Their Binary Mixtures. *JAOCS, Journal of the American Oil Chemists' Society* **1997,** *74*, 1221-1226.

(33)   Lide, D. R., *Crc Handbook of Chemistry and Physics, Internet Version 2005*. CRC Press: Boca Raton, FL 2005;

(34)   Bhushan, B., *Handbook of Micro/Nano Tribology, Second Edition*. Taylor & Francis: 1998;

(35)   Anghel, V.; Cann, P. M.; Spikes, H. A., Direct Measurement of Boundary Lubricating Films. In *Tribology Series*, D. Dowson, C. M. T. T. H. C. C. G. D. Y. B. L. F. J. M. G.; Lubrecht, A. A., Eds. Elsevier: 1997; Vol. Volume 32, pp 459-466.

(36)   El-Shall, H.; Somasundaran, P., Physico-Chemical Aspects of Grinding: A Review of Use of Additives. *Powder Technology* **1984,** *38*, 275-293.

(37)   Morris, H. E., Reactions of Ethyl Alcohol. *Chemical Reviews* **1932,** *10*, 465-506.

(38)   Joly, H. A.; Newton, T.; Myre, M., Activation of C-Cl by Ground-State Aluminum Atoms: An Epr and Dft Investigation. *Physical Chemistry Chemical Physics* **2012,** *14*, 367-374.

(39)   Wang, L.; Guo, Y.; Tsuji, H.; Sakurai, M.; Kameyama, H., Catalytic Oxidation of Dichloromethane over Anodized Aluminum Film. *Journal of Chemical Engineering of Japan* **2006,** *39*, 173-180.

28

(40)   Chen, L.-H.; Huang, C.-C.; Lien, H.-L., Bimetallic Iron–Aluminum Particles for Dechlorination of Carbon Tetrachloride. *Chemosphere* **2008,** *73*, 692-697.

(41)   Ibuki, K.; Nakahara, M., Temperature and Solvent Effects on Viscosity B Coefficients. Monovalent Ions in Acetonitrile at 15, 25, and 35 °C. *Journal of Physical Chemistry* **1990,** *94*, 8370-8373.

(42)   Dymond, J. H.; Oye, H. A., Viscosity of Selected Liquid N-Alkanes. *J. Phys. Chem. Ref. Data* **1994,** *23*, 41-53.

(43)   de Heer, W. A., The Physics of Simple Metal Clusters: Experimental Aspects and Simple Models. *Rev. Mod. Phys.* **1993,** *65*, 611-76.

(44)   Schwartz, M. P.; Hamers, R. J., Reaction of Acetonitrile with the Silicon (001) Surface: A Combined Xps and Ftir Study. *Surface Science* **2007,** *601*, 945-953.

(45)   Schwartz, M. P.; Hamers, R. J., The Role of Pi-Conjugation in Attachment of Organic Molecules to the Silicon (001) Surface. *Surface Science* **2002,** *515*, 75-86.

(46)   Filler, M. A.; Mui, C.; Musgrave, C. B.; Bent, S. F., Competition and Selectivity in the Reaction of Nitriles on Ge(100)-2×1. *Journal of the American Chemical Society* **2003,** *125*, 4928-4936.

(47)   Zhu, Y.-G.; Li, Z.-Q.; Zhang, D.; Tanimoto, T., Structural Changes in Poly(Ethylene Terephthalate) Induced by Cryomilling and Ambimilling. *J. Polym. Sci., Part B: Polym. Phys.* **2006,** *44*, 986-993.

(48)   Chen, S.; Liu, W., Oleic Acid Capped Pbs Nanoparticles: Synthesis, Characterization and Tribological Properties. *Materials Chemistry and Physics* **2006,** *98*, 183-189.

(49)   Robinet, L.; Corbeil, M. C., The Characterization of Metal Soaps. *Studies in Conservation* **2003,** *48*, 23-40.

(50)   Lee, H. M.; Choi, S.-Y.; Yun, J.-Y., Preparation of Aluminum–Organic Nanocomposite Materials Via Wet Chemical Process. *Advanced Powder Technology* **2011,** *22*, 608-612.

(51)   Hou, Y.; Kondoh, H.; Shimojo, M.; Sako, E. O.; Ozaki, N.; Kogure, T.; Ohta, T., Inorganic Nanocrystal Self-Assembly Via the Inclusion Interaction of B-Cyclodextrins: Toward 3d Spherical Magnetite. *J. Phys. Chem. B* **2005,** *109*, 4845-4852.

(52)   Thistlethwaite, P. J.; Hook, M. S., Diffuse Reflectance Fourier Transform Infrared Study of the Adsorption of Oleate/Oleic Acid onto Titania. *Langmuir* **2000,** *16*, 4993-4998.

(53)   Wu, N.; Fu, L.; Su, M.; Aslam, M.; Wong, K. C.; Dravid, V. P., Interaction of Fatty Acid Monolayers with Cobalt Nanoparticles. *Nano Letters* **2004,** *4*, 383-386.

(54)   Bronstein, L. M.; Huang, X.; Retrum, J.; Schmucker, A.; Pink, M.; Stein, B. D.; Dragnea, B., Influence of Iron Oleate Complex Structure on Iron Oxide Nanoparticle Formation. *Chem. Mater.* **2007,** *19*, 3624-3632.

(55)   Trefry, J. C.; Monahan, J. L.; Weaver, K. M.; Meyerhoefer, A. J.; Markopolous, M. M.; Arnold, Z. S.; Wooley, D. P.; Pavel, I. E., Size Selection and Concentration of Silver Nanoparticles by Tangential Flow Ultrafiltration for Sers-Based Biosensors. *J. AM. CHEM. SOC.* **2010**.

(56)   Baker, C. C.; Ceylan, A.; Shah, S. I., Reactive Gas Condensation Synthesis of Aluminum Nitride Nanoparticles. *Journal of Nanoscience and Nanotechnology* **2006,** *6*, 146-150.

(57)   Fu, Q.; Wagner, T., Interaction of Nanostructured Metal Overlayers with Oxide Surfaces. *Surface Science Reports* **2007,** *62*, 431-498.

(58)   Davies, P. R.; Newton, N. G., The Chemisorption and Decomposition of Pyridine and Ammonia at Clean and Oxidised Al(111) Surfaces. *Surface Science* **2003,** *546*, 149-158.

(59)   Schoser, S.; Bräuchle, G.; Forget, J.; Kohlhof, K.; Weber, T.; Voigt, J.; Rauschenbach, B., Xps Investigation of Aln Formation in Aluminum Alloys Using Plasma Source Ion Implantation. *Surface and Coatings Technology* **1998,** *103-104*, 222-226.

(60)   Zähr, J.; Oswald, S.; Türpe, M.; Ullrich, H. J.; Füssel, U., Characterisation of Oxide and Hydroxide Layers on Technical Aluminum Materials Using Xps. *Vacuum* **2012,** *86*, 1216-1219.

(61)   Kwon, Y.-S.; Gromov, A. A.; Ilyin, A. P.; Rim, G.-H., Passivation Process for Superfine Aluminum Powders Obtained by Electrical Explosion of Wires. *Applied Surface Science* **2003,** *211*, 57-67.

(62)   Kloprogge, J. T.; Duong, L. V.; Wood, B. J.; Frost, R. L., Xps Study of the Major Minerals in Bauxite: Gibbsite, Bayerite and (Pseudo-)Boehmite. *Journal of Colloid and Interface Science* **2006,** *296*, 572-576.

(63)   Balchev, I.; Minkovski, N.; Marinova, T.; Shipochka, M.; Sabotinov, N., Composition and Structure Characterization of Aluminum after Laser Ablation. *Mater. Sci. Eng., B* **2006,** *135*, 108-112.

Table 1. Results for milling in non-polar solvents and oleic acid solutions in non-polar solvents Note: **x** indicates that < 1mg produced

Particles produced using non-polar solvent	benzene	n-heptane	toluene	1.7×10^{-5} M OA in toluene	3.0×10^{-5} M OA in toluene	1.0×10^{-2} M OA in toluene	n-hexane	1.6×10^{-1} M OA in hexane
Nanoparticles	x	x	x	x	x	~ 10 mg	x	~ 100 mg
Micron flakes	x	x	x	~ 10 mg	~ 23 mg	~ 500 mg	x	~ 1 g

Table 2. Particle production results for milling in various polar solvents. Note: x indicates that < 1mg produced

Particles produced using polar solvent	Oleic acid	Oleylamine	Benzylamine	Acetonitrile	Ethanol	Dichloromethane
Nanoparticles	~ 100 mg	~ 10 mg	~ 10 mg	~ 1 g		
					~ 5 g Al_2O_3	~ 5 g $AlCl_3$
Micron Flakes	~ 5 g	~ 2 g	~ 3 g	~ 1 g		
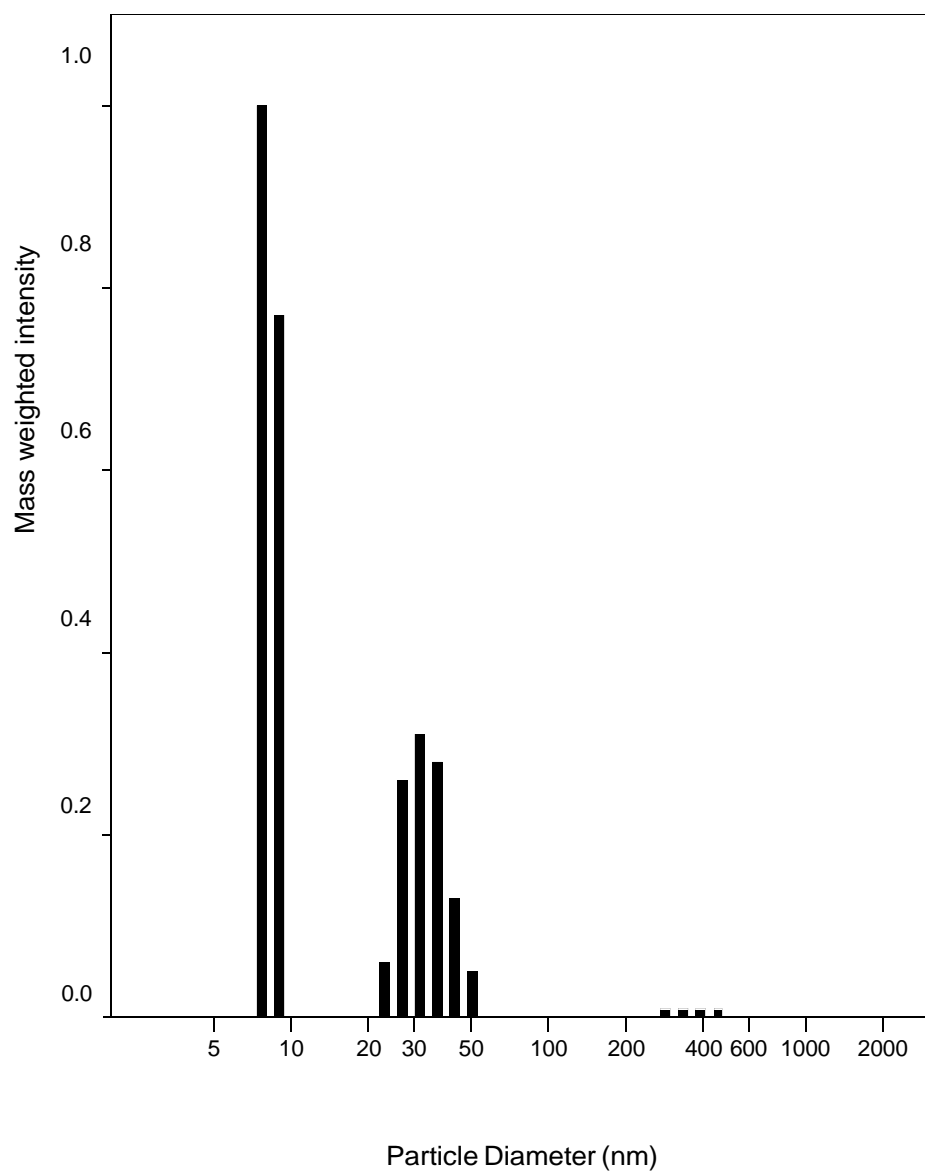
Fig. 1 Dynamic light scattering analysis of aluminum nanoparticles milled in acetonitrile for 3 hours, capped with oleic acid, and redispersed in hexanes
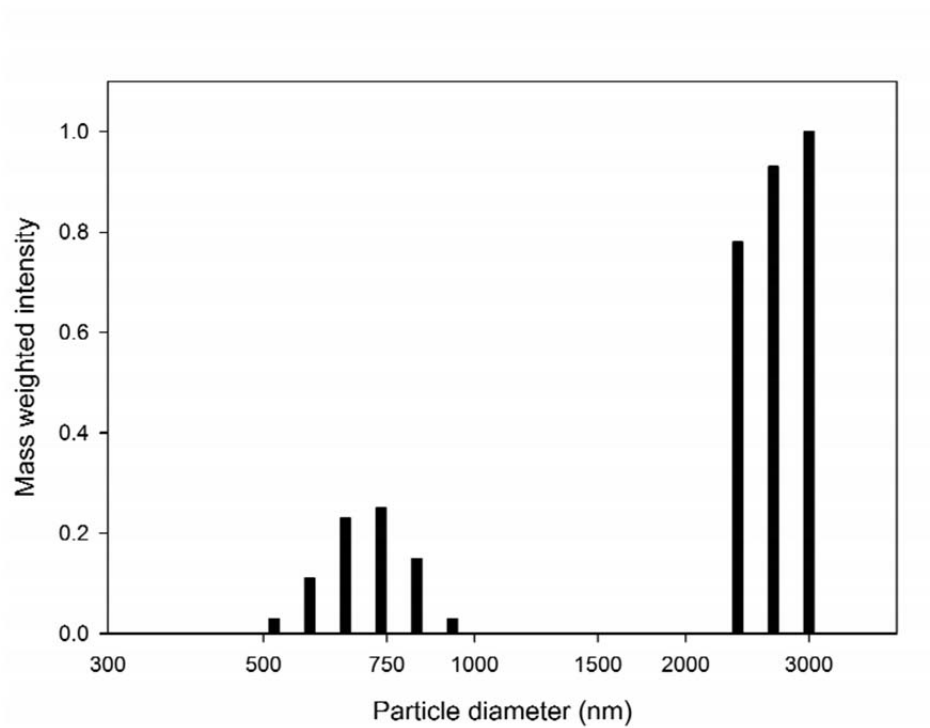
Fig. 2 Dynamic light scattering analysis of the aluminum particles collected by centrifugation
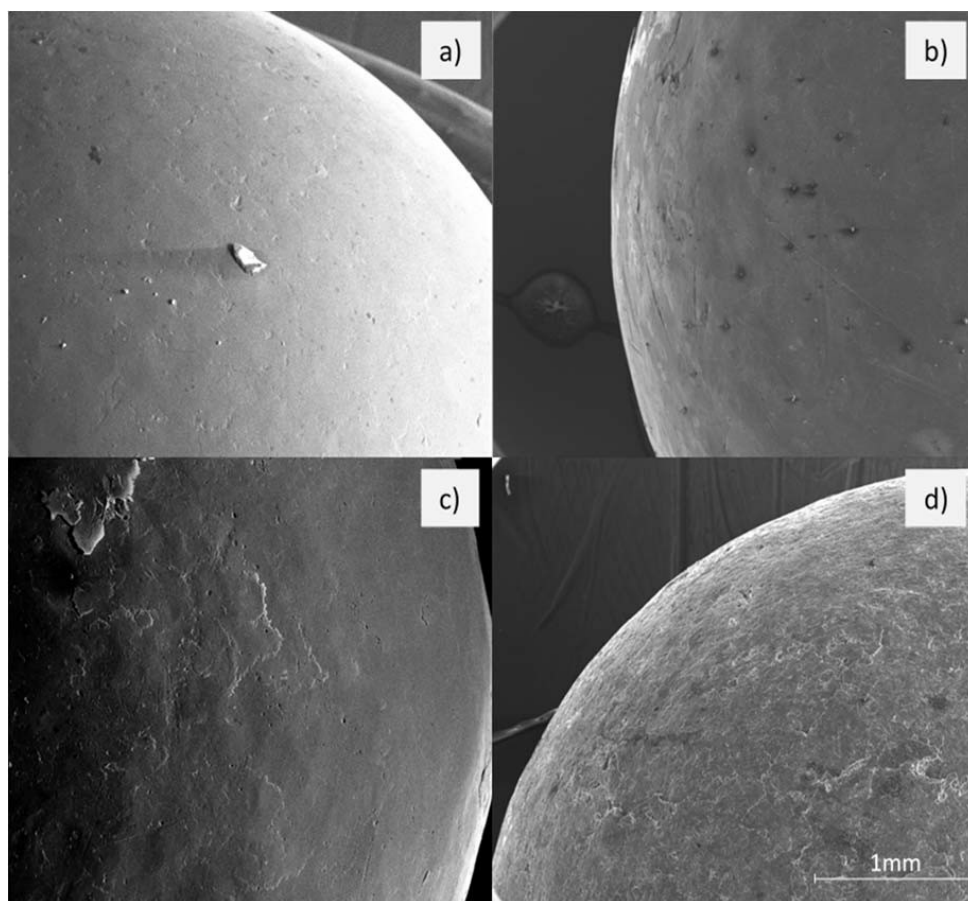
Fig. 3 Scanning electron microscopy images of aluminum balls used in homogeneous media milling: **a)** As-received; **b)** milled 6 hours in neat toluene; **c)** milled 3 hours in 10mM of oleic acid in toluene; **d)** milled 3 hours in acetonitrile
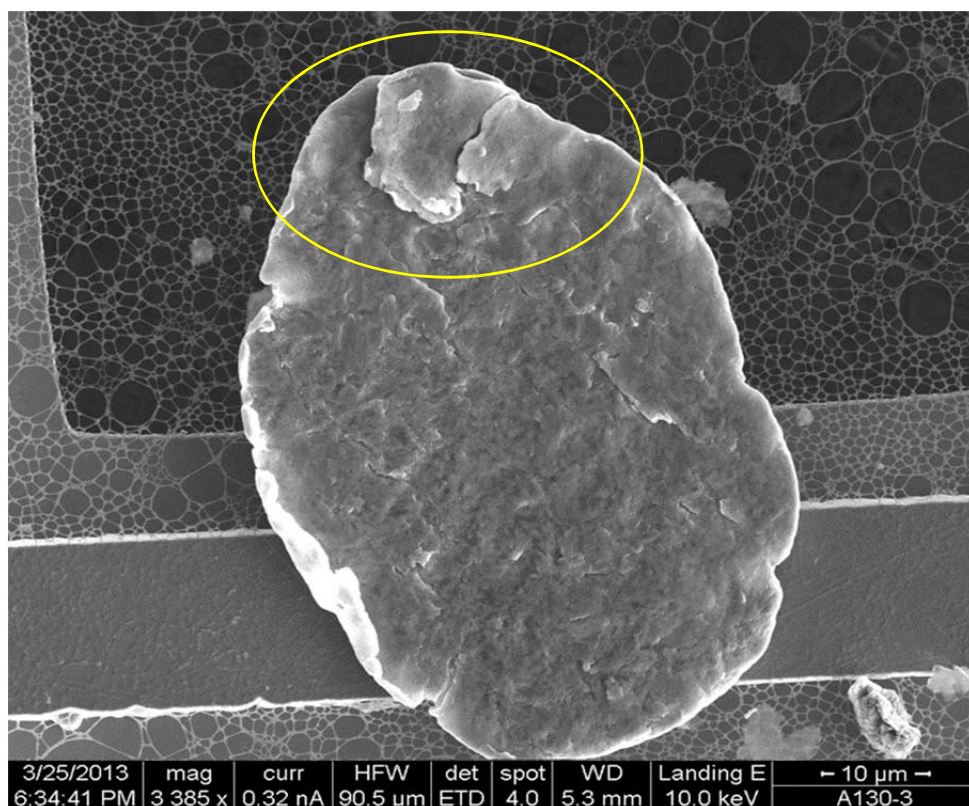
Fig. 4 Scanning electron micrograph (SEM) of a large aluminum flake produced in 15 minutes of acetonitrile milling
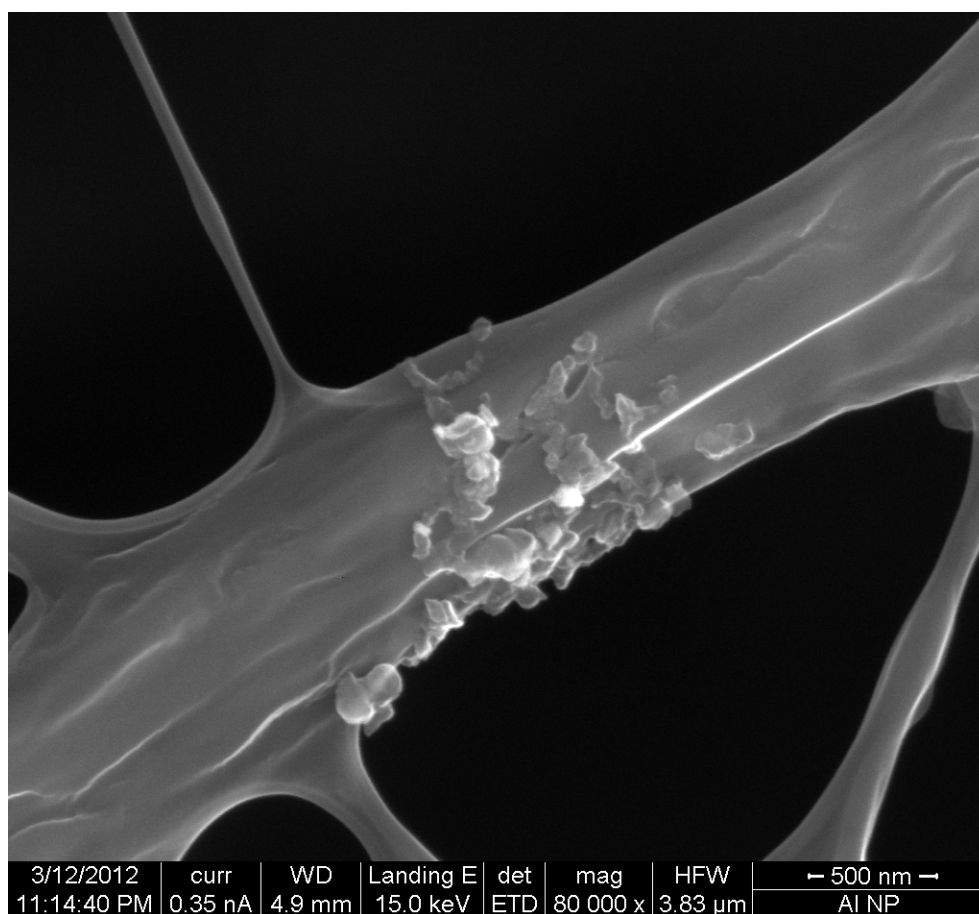
Fig. 5 SEM image of acetonitrile-milled particles, subsequently capped with oleic acid, and deposited on lacey carbon
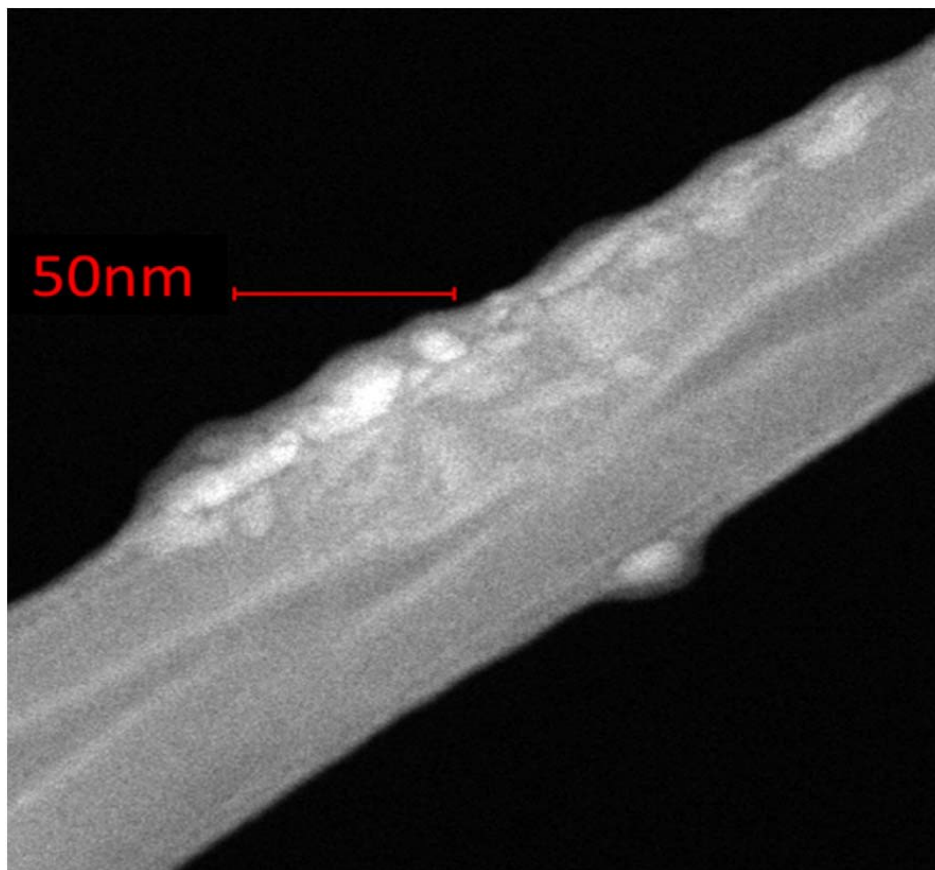
Fig. 6 TEM image of acetonitrile-milled particles, subsequently capped with oleic acid, and deposited on lacey carbon
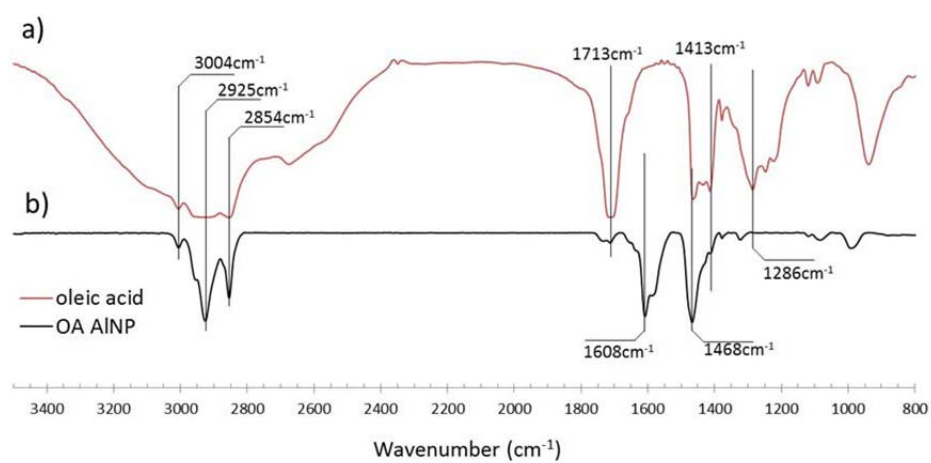
Fig. 7 Reflectance FTIR of a) neat oleic acid; b) oleic acid-capped aluminum nanoparticles

[H/CH₃CO₂/Al₈₀] interactions
M06/6-311++G(d,p) level

Relative energies, kcal/mol (excl. ZPE)

19   0   7
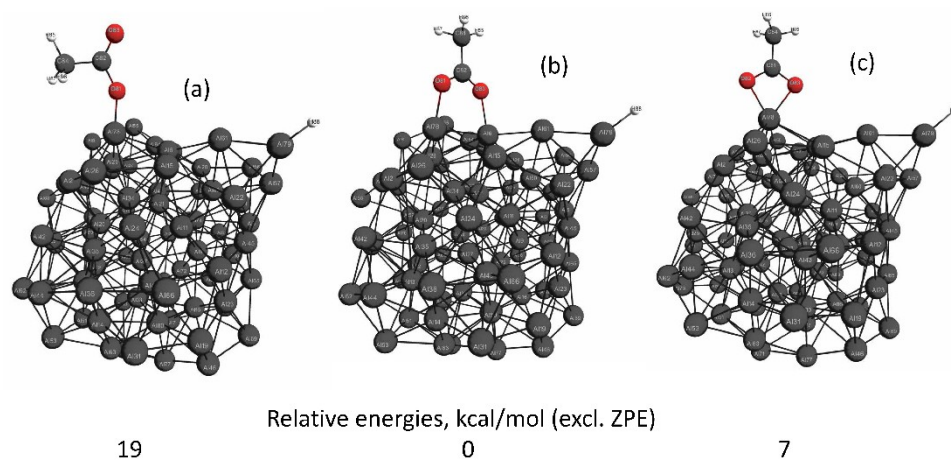
Fig. 8 Relative energies for acetic acid binding to an Al_{80} cluster as calculated using density functional theory with a basis set of M06/6-311++G(d,p)
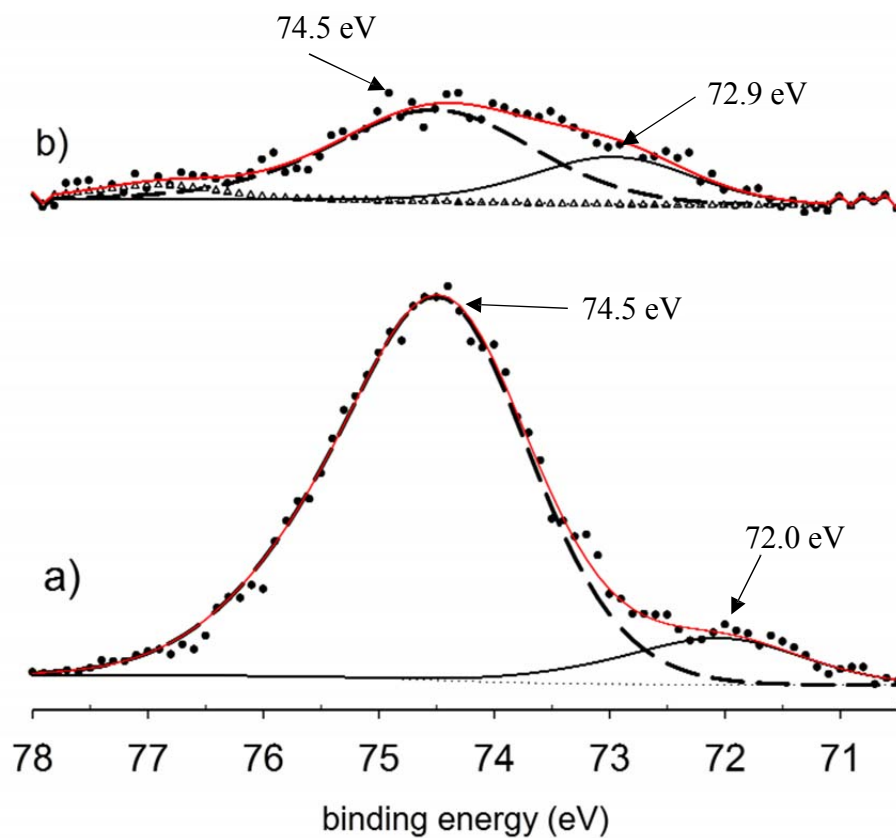
Fig. 9 High resolution scans of the Al 2p peak for: a) acetonitrile-milled aluminum nanoparticles; b) acetonitrile-milled, oleic acid-capped aluminum nanoparticles. Note: both samples were argon sputtered to remove adventitious species.
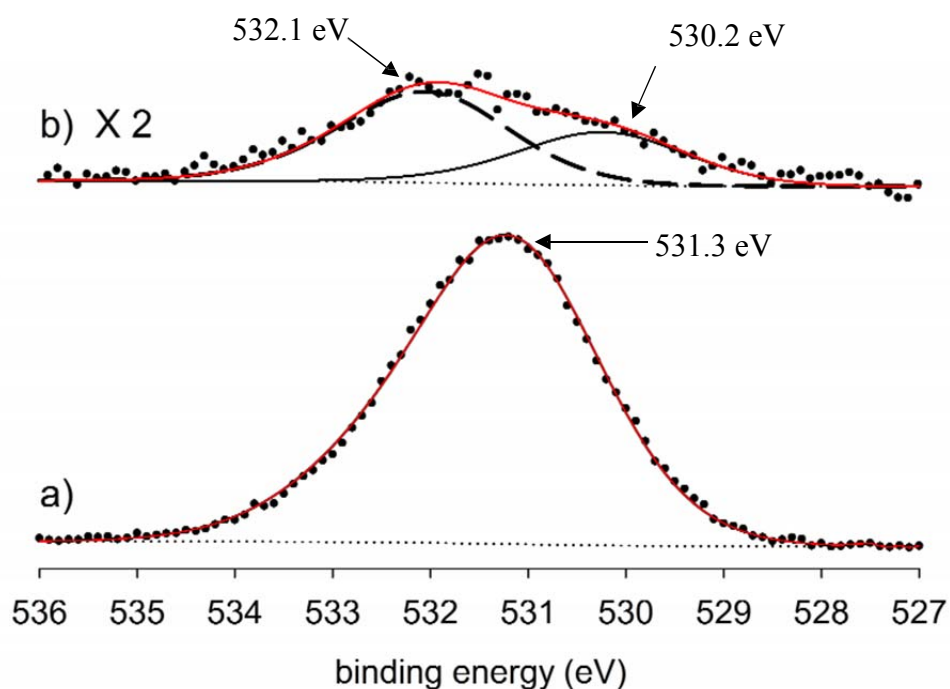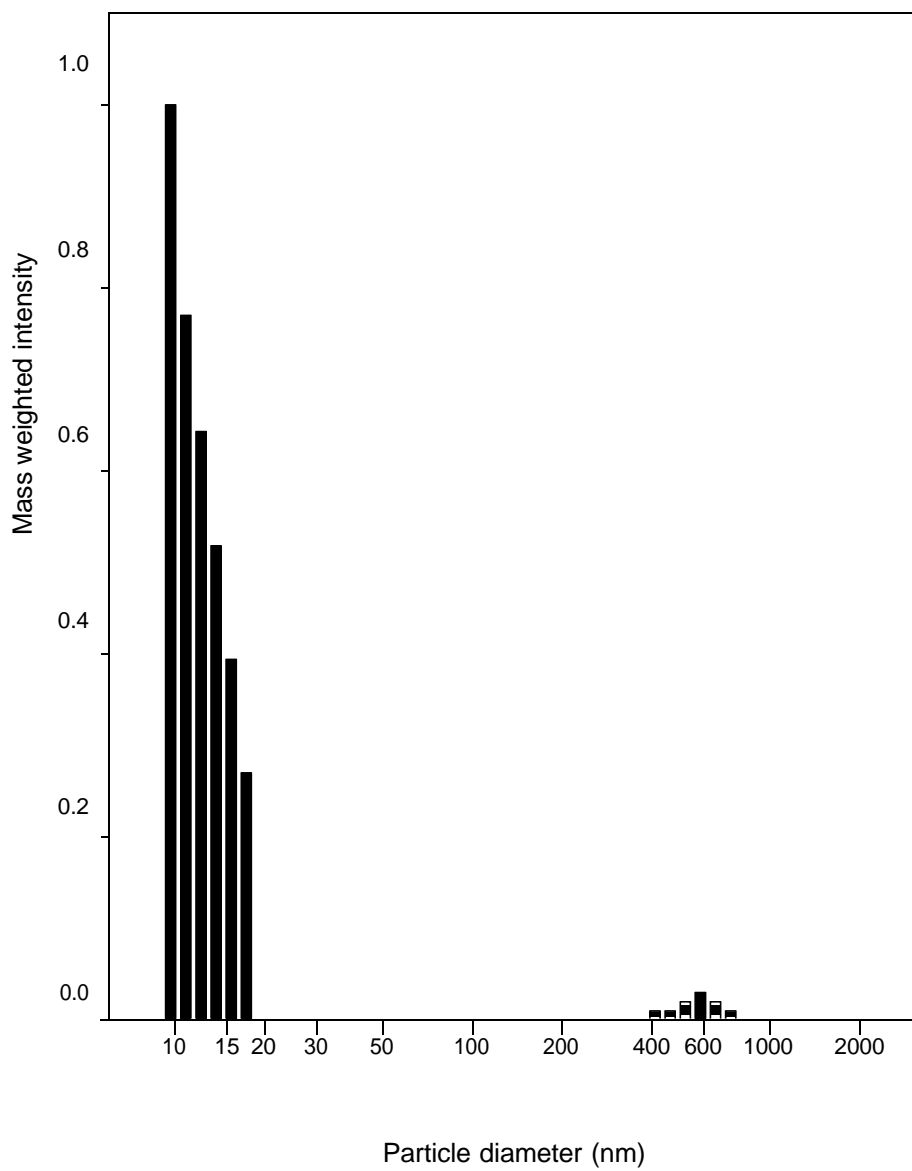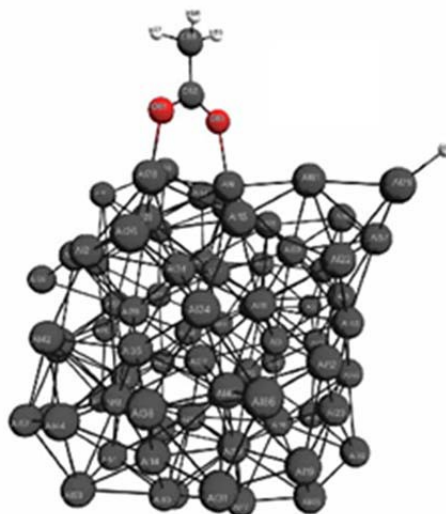
Fig. 10 High resolution scans of the O 1s peak for: a) acetonitrile-milled aluminum nanoparticles; b) acetonitrile-milled, oleic acid-capped aluminum nanoparticles. Note: both samples were argon sputtered to remove adventitious species.
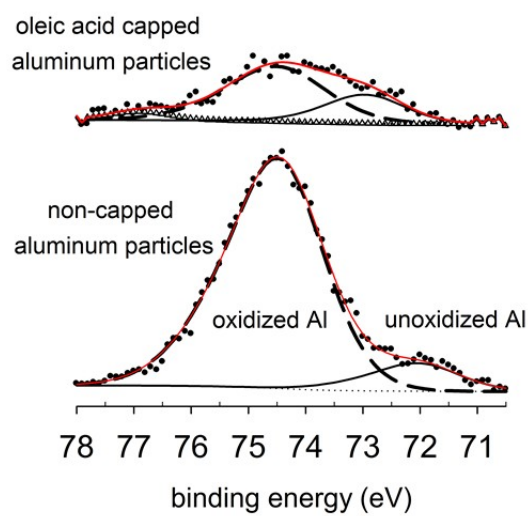
Fig. 11 Mass weighted particle size distribution for oleic acid-capped iron nanoparticles synthesized by milling for 3 hours in 5% oleic acid/hexanes under an argon atmosphere.

TOC only